Fundamentals and Applications of Acoustic Metamaterials

Edited by Vicent ROMERO-GARCíA and Anne-Christine HLADKY-HENNION

November 21, 2018

Contents

Chapter 1

Locally resonant metamaterials for plate waves: the respective role of compressional versus flexural resonances of a dense forest of vertical rods.

Recent experimental and numerical studies have showed that at the geophysics scale, locally resonant metamaterials have potential future applications to seismic engineering. To pursue investigations in geophysics with media that are mostly unknown and heterogeneous, more understanding is needed in terms of the interactions between surface waves with different polarization and the various types of resonance of a unit cell of a metamaterial. Benefitting from an analog experiment at the laboratory scale, this Chapter revisits the interactions between plate Lamb waves and a cluster of long vertical rods – with easy-to-identify compressional and flexural resonances – attached to it. Through densely sampled spatial measurements, particular attention is paid to the analysis of the complex wavefield that results from this combination of resonances, on the dominant Lamb wave mode in the plate.

1.1. Introduction

Locally resonant metamaterials derive their effective properties from hybridization between their resonant unit cells and the incoming wave [LIU 00, PSA 02, FAN 06, GUE 07, LER 09, COW 11, LEM 11, LEM 13, CHR 12, ACH 13, RUP 14]. This

Chapter written by Martin LOTT and Philippe ROUX.

phenomenon is well understood for waves that propagate in media where the unit cells respect the symmetry of the incident field [PEN 99, SMI 00]. However, in many systems, such as a set of vertical rods that interact with plate waves, or a pine tree forest that interacts with surface seismic waves, several modes with orthogonal symmetries can coexist at any given frequency, while the resonant unit cells themselves can support different types of resonance [RUP 15, RUP 17].

In this Chapter, we revisit metamaterial physics at the mesoscopic scale. At the seismic scale, recent studies have demonstrated that trees can behave as seismic resonators with flexural and compressional resonances, whereby a forest of trees represents a seismic-scale candidate for a locally resonant metamaterial for surface waves [BRÛ 14, COL 14, COL 16b, COL 16a, COL 16c, ROU 18]. Spatial sampling in the METAFORET experimental configuration (for details, see: `https://metaforet.osug.fr/`) was performed with a dense array of geophones in and around a pine forest with a typical scale of the order of 100 m (Fig. 1.1a). Mostly surface waves were excited by a vibrometer, with controlled and programmable source signals with horizontal and vertical polarizations that coupled with both flexural and compressional resonances. The goal of the experiment was to establish a link between seismic-relevant scales and microscale and mesoscale studies that pioneered the development of metamaterial physics in optics and acoustics. The main results of the METAFORET experiment were the presence of frequency band gaps for Rayleigh waves associated with compressional and flexural resonances of the trees, which confirmed the strong influence that a dense collection of trees can have on the propagation of seismic waves [ROU 18].

However, the seismic experiment also indicated the need to better understand the respective roles of these resonances on the wavefield pattern in the context of metamaterial physics. We thus proceed by analogy in the present Chapter, going back to the case at the laboratory scale, as a dense set of vertical rods attached to a plate with typical length now of the order of 1 m (Fig. 1.1b). In the context of a locally resonant metamaterial, the plate-plus-rods system allows the study of the respective roles of flexural and compressional resonances on the hybridization of the plate waves, as these resonances induce a break in the orthogonality between the Lamb wave modes of the free plate.

The Chapter is organized as follows. Section 1.2 describes the experimental set-up at the laboratory scale. In Section 1.3, the field pattern issued from point-like sources located either inside or outside the metamaterial are analyzed and discussed in the framework of a simplified theoretical approach, where only one type of Lamb waves in the plate and one type of resonance of the rods (i.e., compressional resonance) are considered. The complete wavefield pattern is discussed in Section III, and the role of flexural resonances of the rods is magnified through different examples.

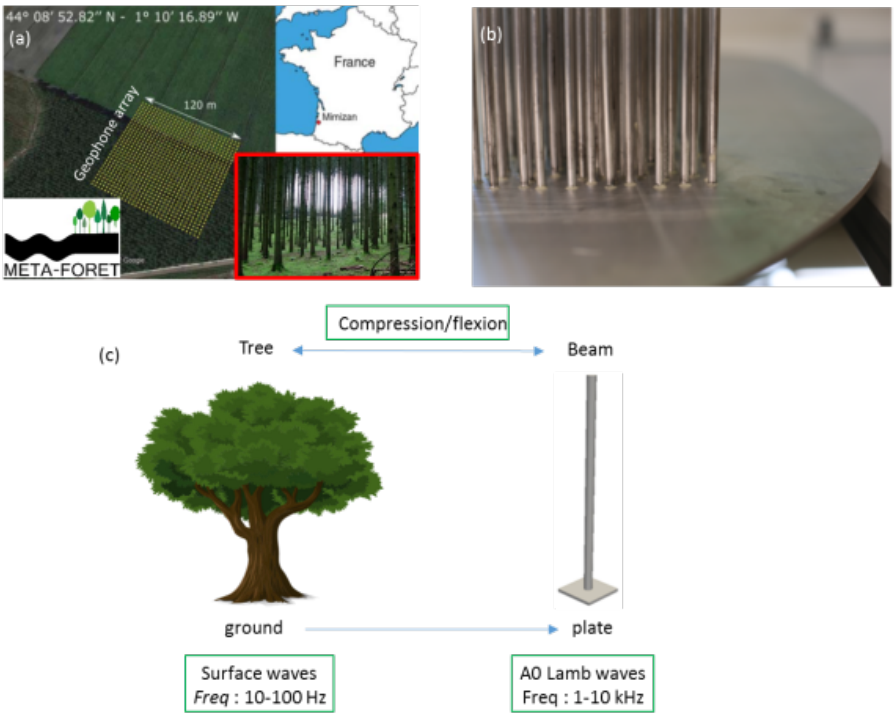

Figure 1.1 – Examples of locally resonant metamaterials at different scales for seismo-elastic waves. (a) Seismic deployment (yellow dot) at the interface between a free field and a dense pine tree forest. (b) Squared area of a random arrangement of vertical metallic rods glued to a thin aluminum plate. (c) Mechanical similitudes of the unit resonant cell for both systems, with their respective frequency bands of interest.

1.2. Experimental configuration of the metamaterial at the lab scale

Throughout this study, analogy is made between the METAFORET seismic experiment and this laboratory scale experiment, as a 'forest' of 61-cm-long, 6-mm-diameter vertical rods attached to a thin metallic plate (Fig. 1.1; for a more general description, see Roux et al. [ROU]). Unlike the seismic configuration, the rods and plate are made of the same material, which provides perfect coupling for wave propagation. At low frequencies (<10 kHz), the 6-mm-width plate supports two types of waves known as the symmetric and anti-symmetric modes, as S_0 and A_0 [ROY 00]. In practice, the A_0 waves are mostly vertically polarized and can be characterized by out-of-plane (vertical) displacement, while in-plane (horizontal) displacements in the plate are described by the S_0 waves. A few point-like piezo sources located either inside or outside the metamaterial are attached to one side of the plate, and these mostly excite A_0 Lamb

waves. The spatial arrangement of the rods is random, and the average distance d between rods is such that $10 < d/\lambda < 4$, where λ is the A_0 wavelength in the plate over the frequency band of interest.

With this experimental configuration, only the out-of-plane wavefield can be measured on the plate, through a motorized laser vibrometer that covers a large surface inside and outside the metamaterial area, as depicted schematically in Fig. 1.2. The received signals are highly dispersed because of reverberation at the plate boundaries. Attenuation in the metallic plate is low for the A_0 waves. The billiard-table shape of the plate makes the field spatially random after a few reverberations from the plate boundaries. As will be shown later, these reverberations are of great importance for both array analysis and frequency-time analysis of the received signals in the metamaterial.

This laboratory scale configuration allows us to carefully study the roles of the flexural and compressional resonances inside the forest of rods for the out-of-plane wavefield measured on the plate surface. In the [1 kHz, 10 kHz] frequency bandwidth, the wave propagation in the complex plate-plus-rod system deals with S_0 and A_0 modes in the free plate and two types of resonance – flexural and compressional resonance – that should mostly couple with the S_0 and A_0 waves, respectively.

In parallel with the experimental work, numerical simulations performed with three-dimensional elastic finite-element code in the plate-plus-rod metamaterial confirm that when a vertical force with out-of-plane polarization excites the 6-mm-width metallic plate, there is almost no energy in the S_0 mode [COL 14]. This means that to a first approximation, the potential conversion of the excited A_0 waves to S_0 modes upon scattering of the resonating beams can be neglected in this plate-plus-rod configuration.

We expect things to be very different with a thinner plate (i.e., more flexible), where both in-plane and out-of-plane wavefield components can be excited through bending and flexural moments at the interface between the plate and the rods. In such a case, both flexural and compressional resonances can modify the bandgap structure, which would require the addition of the in-plane component to the theoretical approach, as described by Colquitt et al. [COL 17].

In Fig. 1.2d, the spatially averaged Fourier spectra measured both outside and inside the disordered metamaterial reveals two wide band gaps, which start at 2 kHz and 6 kHz.Rupin et al. [RUP 14] showed that the shape and intensity of the band gaps are independent of the random organization of the rods. As expected, when calculated in the passband, the spectral intensity of the reverberated fields are similar inside and outside the metamaterial.

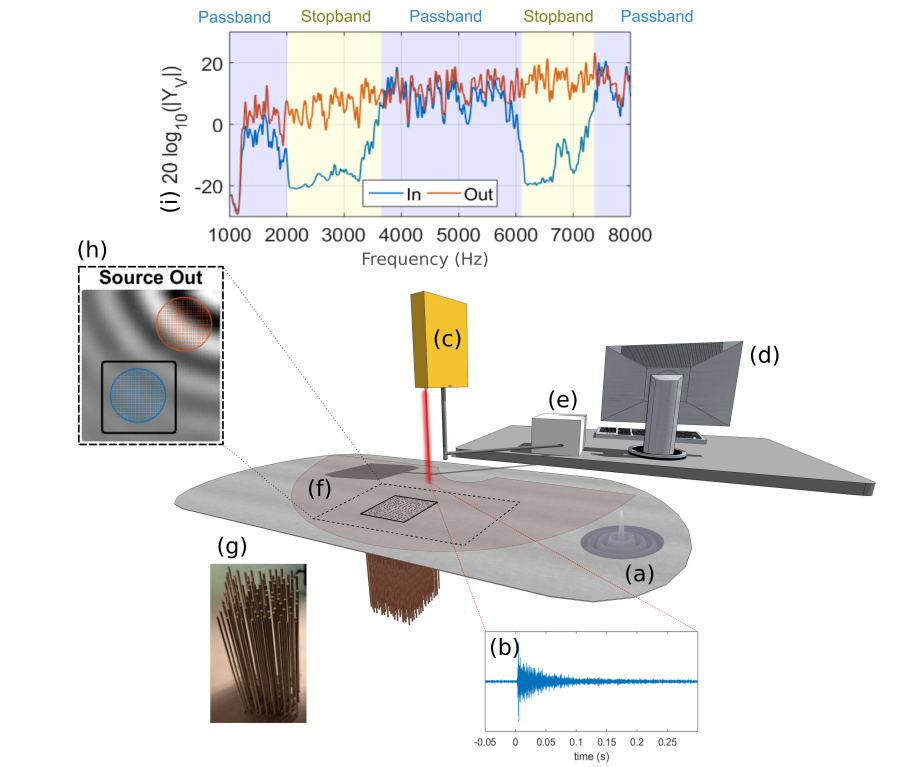

Figure 1.2 – Experimental set-up at the laboratory scale. A piezo-electric point-like source (a) generates A_0 Lamb waves in the aluminum plate. The particle velocity (b) is measured using an out-of-plane laser Doppler velocimeter (c) attached to a PC-controlled (d) motorized robot arm (e). The spatial cover of the robot onto the plate is shown in red (f). The metamaterial (g) is made of 100 vertical rods glued to the opposite side of the plate (black square). The Fourier analysis of the strongly reverberated wavefield (h) measured on the plate surface either inside (in blue) and outside (in red) the forest of rods shows both wide frequency passbands and stopbands where no energy penetrates inside the metamaterial (i).

1.3. Interpretation of dispersion curve restricted to the rod compressional resonances

Taking advantage of the spatially uniform two-dimensional sampling of the wavefield in the metamaterial region, the effective properties of the wave propagation of the A_0 Lamb waves inside the metamaterial were described by Rupin et al. [RUP 14] in the following way. Considering successive time windows associated with long-term

reverberations, and when filtered in a small bandwidth, the averaged spatial Fourier transforms of the field recorded inside the metamaterial revealed a circle, which confirms the equi-distribution of the wave components for all possible azimuthal directions. At each frequency, the circle radius gives an accurate measure of the effective velocity inside the metamaterial, from which the dispersion curve can be plotted (for more details, see Fig. 6.6 in Roux et al. [ROU]).

In the present study, we proceed differently. We calculate the ensemble-averaged two-point correlation function $C(\omega, \mathrm{d}r)$ at pulsation ω, and for all possible receiving points separated by distance $\mathrm{d}r$ inside the metamaterial. The two-point correlation functions are calculated between points $\overrightarrow{r}$ and $\overrightarrow{r}+\mathrm{d}\overrightarrow{r}$ inside the metamaterial area:

$$C_T(\omega, \mathrm{d}\overrightarrow{r}) = \frac{\langle \Psi_T(\omega, \overrightarrow{r}) \Psi_T^*(\omega, \overrightarrow{r} + \mathrm{d}\overrightarrow{r}) \rangle_{\overrightarrow{r}}}{\langle \mid \Psi_T(\omega, \overrightarrow{r}) \mid^2 \rangle_{\overrightarrow{r}}}, \tag{1.1}$$

where $\Psi_T(\omega, \overrightarrow{r})$ is the field measured from the laser vibrometer at pulsation ω for a finite-duration recorded window of duration ΔT, starting at time T. We then take advantage of the equi-distribution of the spatial wavefield inside the ergodic cavity-like plate, by averaging the two-point correlation over all azimuth θ:

$$C_T(\omega, \mathrm{d}\overrightarrow{r}) = \langle C_T(\omega, \mathrm{d}\overrightarrow{r}) \rangle_\theta. \tag{1.2}$$

Finally, we also benefit from the long-term reverberation of the wavefield inside the plate to select as many time windows T as are available, each of which is interpreted as a different source realization for the two-point correlation function:

$$C(\omega, \mathrm{d}\overrightarrow{r}) = \langle C_T(\omega, \mathrm{d}\overrightarrow{r}) \rangle_T. \tag{1.3}$$

Thus, the ensemble-averaged two-point correlation function results from three different averaging process: (1) from the set of positions (x, y) of all of the receiving points inside the metamaterial from which inter-distances $\mathrm{d}r$ are calculated; (2) from a set of five piezo-sources located outside the metamaterial area; and (3) from the long reverberation time T of the strongly reverberated wavefield inside the cavity. In practice, we choose $\Delta T = 10$ ms, which is small compared to the total reverberation time of the cavity (> 250 ms), and T expands from 10 ms (for the wave mixing to be sufficient) to 250 ms (where ambient noise starts to dominate).

The real part of the two-point correlation function $C(\omega, \mathrm{d}r)$ is plotted in Fig. 1.3a at frequency f = 5000 Hz, and for all frequencies inside and outside the metamaterial in Fig. 1.3(b, c). In Fig. 1.3b, the normalization coefficient calculated for the denominator of Eq. 1.1 is plotted (black line) from the averaged intensity measured from

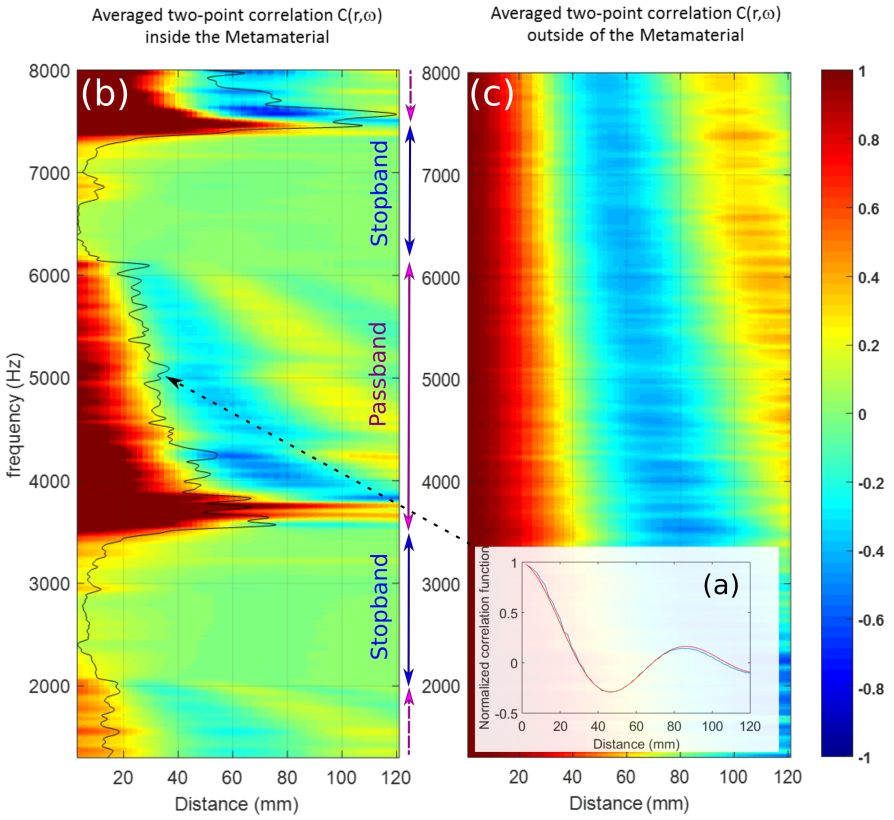

Figure 1.3 – (a) Real part of the averaged two-point correlation function (normalized) measured at 5 kHz for all of the receiver pairs located inside the metamaterial region (blue). The modeled plate Green's function is plotted in red. (b) Averaged two-point correlation versus frequency measured inside the metamaterial (c) and outside the metamaterial. The black line in (b) corresponds to the averaged intensity versus frequency measured inside the metamaterial.

all receiving points inside the metamaterial. This explains why reaches higher values in the passband (where the wavefield propagates inside the metamaterial) than in the stopband (where almost no energy penetrates into the metamaterial).

We then model $C(\omega, \mathrm{d}r)$ calculated in the passbands with the two-dimensional Green's function for an infinite plate $G_0(\omega, \mathrm{d}r)$ defined from the Bessel and Hankel functions of the second kind [FAH 04] as:

$$C(\omega, \mathrm{d}r) \propto G_0(\omega, \mathrm{d}r) = H_0^{(2)}(k_B \mathrm{d}r) - i\frac{2}{\pi} K_0(k_B \mathrm{d}r), \tag{1.4}$$

where $k_{eff} = \omega / c_{eff}$ is the effective propagating wavenumber of the A_0 waves with effective velocity $c_{eff} = \Re(c_{eff}) + i\Im(c_{eff})$. In practice, $\Re(c_{eff})$ corresponds to the effective velocity for wave propagation, and $\Im(c_{eff})$ is linked to the scattering attenuation (as the intrinsic attenuation is negligible here), and provides a measurement of the elastic mean free path $\frac{\mid c_{eff} \mid^2}{\omega \Im(c_{eff})}$, which is classically defined in multiple scattering field theory as the attenuation of the coherent wavefield [DER 01a, DER 01b]. In Fig. 1.4a, the wave propagation properties in the passband of the metamaterial are summarized as a single dispersion curve (blue dots) computed as $\tilde{k}_{eff} = \Re(k_{eff}) = \frac{\omega \Re(c_{eff})}{\mid c_{eff} \mid^2}$. The dispersion relations of the A_0 Lamb mode calculated with the same procedure outside the metamaterial area is superimposed for comparison (purple dots). The mean free path l in the passband (not shown here) is much larger than the effective wavelength, as $\tilde{k}_{eff} l \gg 1$, which confirms that no scattering attenuation pollutes the wavefield in this frequency band.

In recent years, we have developed an analytical approach to describe the physics properties of multi-resonant metamaterials for Lamb waves propagating in plates (see Ref. [WIL 15]). This theoretical approach neglects the in-plane wavefield component (which cannot be measured by the laser vibrometer) and the flexural resonance of the rods. The metamaterial consists of a 10×10 uniform, periodic array of long rods attached to the surface of a plate that forms the substrate in which anti-symmetric A_0 Lamb waves are excited. It was then shown that the A_0 Lamb wave propagation through the metamaterial can be accurately modeled using a simplified approach that replaces the two-dimensional array with a one-dimensional beam with a linear array of 10 rods. The wave propagation problem is solved rigorously for this one-dimensional system by formulating a scattering matrix at a single rod, found from the boundary conditions at the rod/ beam interface, and including both evanescent and propagating waves in the beam. To predict the transmission through the linear array of rods, this scattering matrix is used to set up an eigenvalue problem, along with the boundary conditions between the adjacent unit cells. The eigenvalues are determined exactly, and then they are approximated to a long wavelength expansion to determine the simple expression for the effective wavenumber k_{eff} :

$$k_{eff} = k_p \left[\frac{M_b}{M} \frac{\tan(k_b L_b)}{k_b L_b} + 1 \right]^{1/4}. \tag{1.5}$$

In Eq. 1.5, k_p is the A_0 wavenumber in the free plate, M_b is the total mass of a rod, and M is the mass of the $L \times L$ plate area, where L = 2 cm corresponds to the averaged inter-rod distance, with $M_b / M = 8.02$ in the present configuration. Finally, the rod

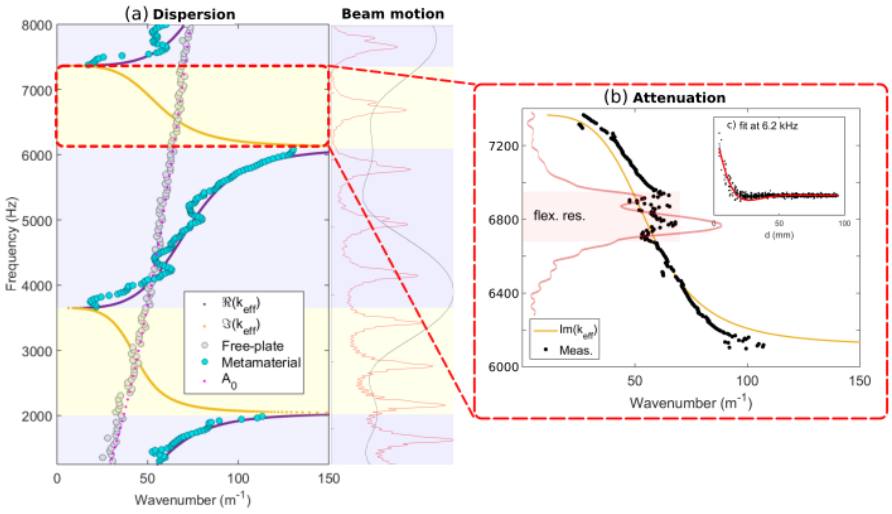

Figure 1.4 – Frequency-wavenumber representation of the plate-plus-rods system. (a) The dispersion curves are obtained for a source outside the metamaterial, and are computed from the averaged two-point correlation function inside (blue dots) and outside (grey dots) the metamaterial region. Theoretical results are represented with solid purple (passband) and yellow (stopband) lines. (b) The attenuation inside the second bandgap is computed from a source located within the metamaterial region. The inset shows the real part of the wavefield at frequency f = 6400 Hz for every receiver, as a function of the distance to the source.

length is L_b = 61 cm, and we have $k_b = \omega/c_b$ with c_b defined as the nondispersive wave velocity in the rod, calculated from Young's modulus E_b and density ρ_b, such that $c_b = 5055$ m.s^{-1}.

The dispersion relation shows bending and anti-bending branches that are modeled through a tangential dependence on the rod length. Both the rod length and the additive mass on the plate drive the hybridization effect of this locally resonant metamaterial.

In Fig. 1.4a, the modeled dispersion relation (purple line) is compared to the experimental dispersion curve (blue dots) inside the metamaterial, as calculated from $C(\omega, \mathrm{d}r)$, with excellent agreement demonstrated. When the set of multi-resonant rods is restricted to compressional vibrations that have similar polarizations as the A_0 Lamb wave out-of-plane displacements in the plate, this produces two wide stopbands in the frequency domain from 0 kHz to 10 kHz. Note that the stopband and passband boundaries depend on the minima and maxima of the rod impedance (Fig. 1.5c),

calculated as a vertical force on the plate, as shown by Williams et al. [WIL 15]:

$$Z_b = -i\rho_b A_b c_b \tan(k_b L_b), \tag{1.6}$$

where A_b is the cross-section of one rod.

To confirm this result, the rod response is measured at the tip of a single rod that is attached to the plate but isolated from the metamaterial (Fig. 1.5a). One accelerometer is attached at the tip of the rod, to measure the vertical displacement of the field inside the rod (black arrow). The flexural motion of the rod is measured using a laser vibrometer that is horizontally directed toward the rod tip (red arrow). A set of three accelerometers are glued to the plate at the bottom of the rod, to deconvolve the plate motion from the rod response.

When excited by a piezo source attached to the plate in the far field, the rod response shows both low-Q compressional resonances measured from the vertical motion captured at the accelerometer, and high-Q flexural resonances measured from the horizontal motion recorded by the laser vibrometer (Fig. 5b). COMSOL simulation was performed for a single rod attached to the free plate, and this provides the modal deformation both along the rod and on the plate at three frequencies close to the flexural or compressional resonances (Fig. 1.5(d-f)). Two observations can be made from these numerical simulations. First, the modal deformations of the single rod in Fig. 1.5(e, f) are in agreement with the forced free-impedance calculations (Eq. (1.6)) obtained in the framework of the theoretical approach (Fig. 1.5c) led by Williams et al. [WIL 15], which confirms the point-like normal force behavior of each rod of the metamaterial on the plate at these frequencies. Secondly, the plate deformation is maximal at a frequency close to the start of the passband (i.e., compressional resonance; Fig. 1.5e) and minimal at a frequency close to the start of the stopband (i.e., compressional anti-resonance; Fig. 1.5f). When generalized to the metamaterial behavior, the plate would appear to be clamped (i.e., no displacement) at the start of the bandgap, and on the contrary, the plate would be allowed to move freely (i.e., maximum displacement) at the start of the passband. Again, this is in agreement with the general wave phenomena observed with the plate-plus-rods system.

When compared to the dispersion curve in Fig. 1.4, we observe that the bandgap starts almost at the anti-resonance, and ends almost at the resonance of the rod impedance, as expected from Eq. (1.5). The 'almost' here is determined by the distance between the beams (or more precisely, the average square root of the mean surface occupied by a beam in the metamaterial) and the mass of the beam M_b, through the M_b/M ratio in Eq. (1.5). At the anti-resonance (Fig. 1.5e), the plate appears to be clamped by the collection of rods, and no motion is allowed in the metamaterial region, which defines the start of the bandgap. On the contrary, the plate motion induced by the bar is maximal at the resonance (Fig. 1.5d), which means that the metamaterial no longer prevents propagation of A_0 Lamb waves in the plate.

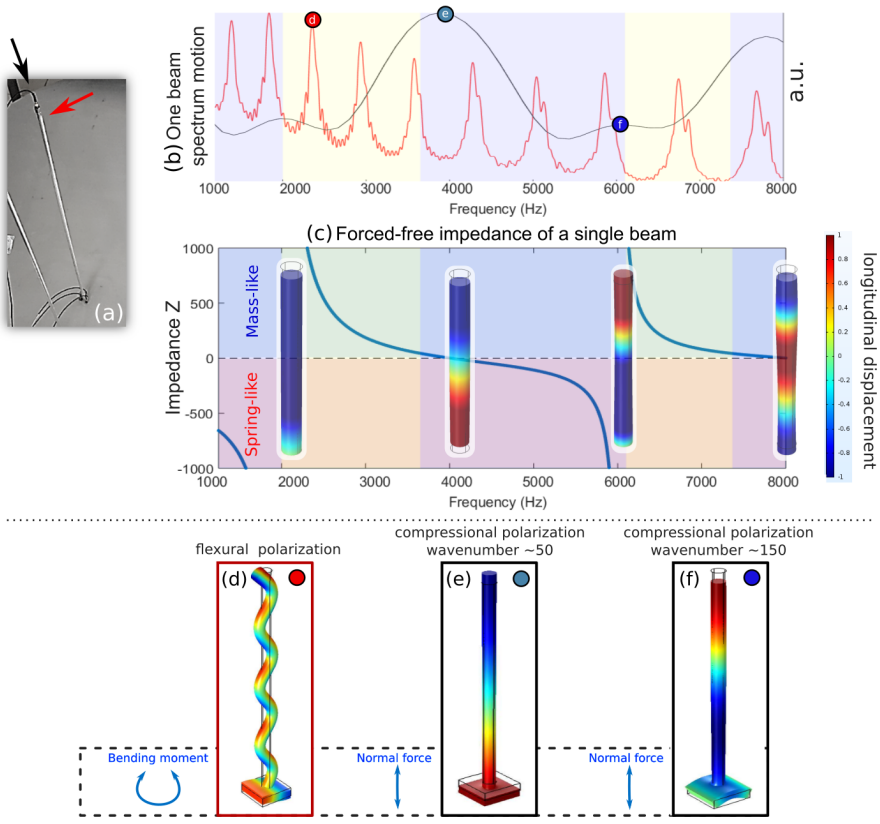

Figure 1.5 – Impedance and mechanical coupling of a single rod attached to the plate. (a) Instrumentation of a single rod for longitudinal (black arrow) and flexural (red arrow) motion. (b) Spectrum motion of a single rod. the out-of-plan motion is shown in black, and the in-plan motion in red. (c) Driving point impedance calculation at the base of a single rod attached to the plate, when the rod displacement is limited to longitudinal (vertical) motion. (d-f) Bloch-waves polarization obtained from COMSOL simulation for a single rod attached to a plate, and extracted at different frequencies close to the compressional or flexural resonances.

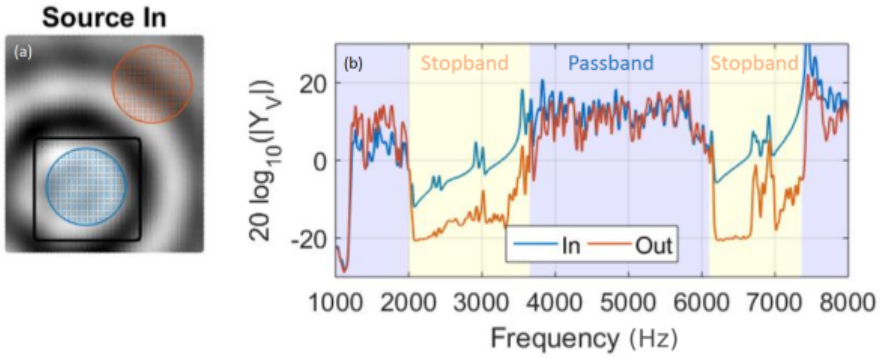

Figure 1.6 – Radiated field from the source inside the metamaterial (black square) together with where the energy averaging is performed (blue, red circles). (b) The averaged energy inside the metamaterial region (blue), and the averaged energy transmitted outside the metamaterial region (red).

In a second step, the piezo source is placed at the center of the metamaterial, to better understand and characterize the wave propagation in the frequency bandgap (Fig. 1.6a). As in Fig. 1.1 for a source outside the metamaterial, the average spectral intensity is computed over the whole frequency bandwidth for the source inside (Fig. 1.6b). In the stopbands, the spectral intensity is now higher inside the metamaterial. Note also the presence of spectral peaks in the stopbands that correspond to the flexural resonances of the rods, the importance of which in the complete description of the plate-plus-rod system will be discussed in Section 1.4.

In Fig. 1.7, the field pattern is plotted at frequency f = 6400 Hz (inside the stopband, but distant from flexural resonance) when the source is located either outside or inside the metamaterial. For the source located outside the metamaterial (Fig. 1.7a), the spatially uniform speckle pattern carries the footprint of the wavefield reverberation in the finite-size plate, and as expected, no field penetrates inside the metamaterial.

This confirms the isotropic behavior of the metamaterial with a random distribution of rods at the subwavelength scale. When the source is located inside the metamaterial (Fig. 1.7b), the wavefield intensity is trapped around the source position in r_0 as an evanescent wave, and as confirmed from the spectral intensity in Fig. 1.6b, no energy escapes from the metamaterial. A new experiment was performed with a finer spatial sampling, as in Fig. 1.7(a, b) ($\Delta x = \Delta y$ = 8 mm in Fig. 1.7(a, b); $\Delta x = \Delta y$ = 4 mm in Fig. 1.7c) on a zone restricted to the metamaterial area (Fig. 1.7c).

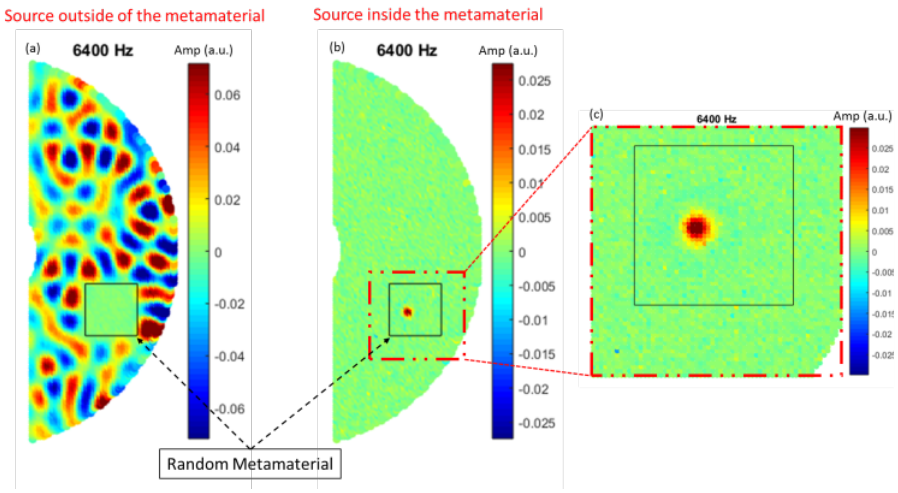

Figure 1.7 – Spatial representation of the Fourier transform (real part) of the wavefield at f = 6400 Hz. The spatial sampling in the x and y directions is 8 mm, and the source is located outside the metamaterial (black square). (b) As for (a), with the source inside the metamaterial. (c) New experiment restricted to the metamaterial region (red dashed square in (b)) with a source at the same position and a spatial sampling in the x and y directions of 4 mm. The source behaves as a monopole in the stopband.

In FIg. 1.4c, the real part of the wavefield is plotted as a function of the distance to the source in r_0 at frequency f = 6400 Hz. In the absence of reverberation, this function is modeled as the two-dimensional Green's function for the plate, as calculated previously (Eq. (1.4)), with $dr = \mid \overrightarrow{r} - \overrightarrow{r}_0 \mid$. As evanescent waves dominate the wavefield around the source, we now have $\tilde{k}_{eff} l \sim 1$, which means that the attenuation length inside the metamaterial is larger than the wavelength of the propagating waves. In practice, Williams et al. [WIL 15] predicted from their theoretical approach that $\tilde{k}_{eff} = \mid \Re(k_e ff) \mid = \mid \Im(k_{eff}) \mid$ in the stopband, which is confirmed by our experimental results obtained with a source inside the metamaterial (Fig. 1.4b). Note, however, that the presence of flexural frequencies disrupts the match of the experimental wavenumber results for $\tilde{k}_{eff}$ with the theoretical approach limited to A_0 Lamb waves interacting with compressional resonances.

1.4. The role played by flexural resonances of the rods

As the main physical properties of the locally resonant metamaterial have been explained from the coupling of the vertically polarized A_0 waves and compressional resonances in the rod, what might be the role of the flexural resonances in the complete description of the plate-plus-rod complex wave system? To define this, the same

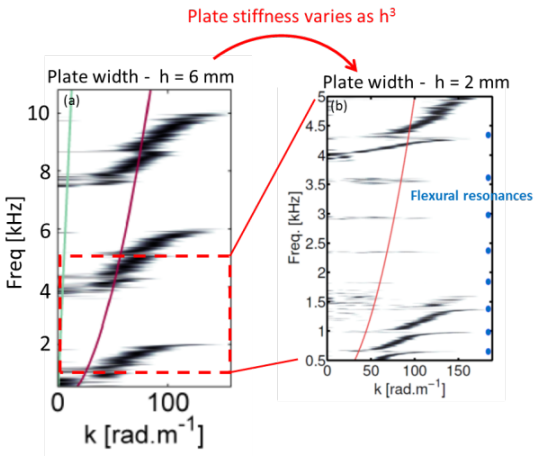

Figure 1.8 – Influence of plate stiffness on the coupling between the rods and the plate at flexural resonances. (a) Dispersion curve obtained experimentally with h = 6-mm-wide plate. (b) As for (a), with an h = 2-mm-wide plate on a restricted part of the frequency spectrum (red dashed square in (a)). For the thinner plate, the plate-plus-rod system shows a stronger interaction with the flexural resonances of the rods, inside and outside the frequency bandgaps.

experiment was performed with a plate of width h = 2 mm (instead of h = 6 mm previously), with a finite bandwidth approach limited to the first bandgap between 0.5 kHz and 5 kHz (Fig. 1.8). As the plate stiffness varies as h^3, the wavefield on the 2-mm plate is expected to be more sensitive to bending motions induced by the vertical rods on the plate [RUP 15, ROU]. This effect is clearly observed for the dispersion curve $\tilde{k}_{eff}$ measured inside the forest of rods attached to this plate with lower stiffness (Fig. 1.8b). Sub-bending and sub-anti-bending branches are observed in the previously defined passbands ($<$2 kHz, $>$4 kHz) at each flexural resonance of the rod, which means that the flexural motion of the rods can no longer be omitted from the interpretation of the dispersion curve. In a similar way, we also observe that flexural resonances lead to transmission bands inside the main bandgap, which means that waves can both penetrate and escape from the metamaterial region using the coupled in-plane/out-of-plane bending motion induced at the points where the rods are attached to the plate (Fig. 1.5d).

These two effects are illustrated for the experimental results given in Figs. 1.9 and 1.10. The wavefield at frequency f = 6700 Hz inside one stopband is shown in Fig. 1.9(a, b) for two separate experiments with point-like sources located inside the metamaterial. In Fig. 1.9b, the source is located at the same position as in Fig. 1.7c. Compared to Fig. 1.7c, where only local evanescent waves were observed,

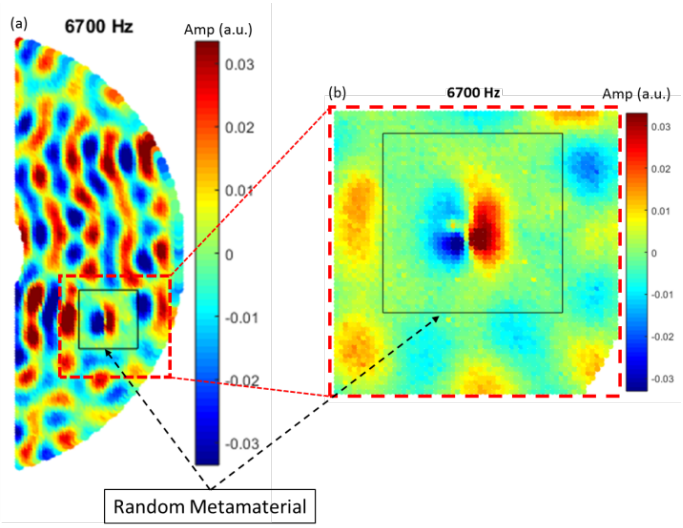

Figure 1.9 – Spatial representation of the Fourier transform (real part) of the wavefield at f = 6700 Hz. (a) The wavefield pattern shows energy leakage in a stopband through one flexural resonance. The source is located inside the metamaterial (black square) and the spatial sampling in the x and y directions is 8 mm. (b) New experiment restricted to the metamaterial region (red dashed square in (b)) with better spatial sampling (4 mm). The source behaves as a dipole at the flexural resonance of the rods.

the presence of a flexural resonance frequency of the rods at f = 6700 Hz (see Fig. 1.5b) completely modifies the wavefield pattern. First, the wavefield is no longer trapped inside the metamaterial, and we observe some energy leakage outside the metamaterial, as expected from the averaged spectral density shown in Fig. 1.6b. Secondly, the wavefield around the source behaves as a dipole instead of a monople, as previously observed for the bandgap only 300 Hz away (Fig. 1.7(b, c)). This dipolar pattern is in agreement with the flexural deformation of the rods that is excited by evanescent waves emitted by the source inside the metamaterial that favor a bending motion of the plate (Fig. 1.5d).

No interpretation of the shape of the dipole can be given at this stage, as this probably depends on the local (but random) organization of the rods around the local source. Note that this dipolar pattern can be observed at each flexural resonance frequency of the rods inside the stopband. In other words, since the out-of-plane A_0 type mode is forbidden inside the metamaterial, the low-amplitude flexural waves locally excited by evanescent waves at the rod/ plate interface can now be observed with an obvious

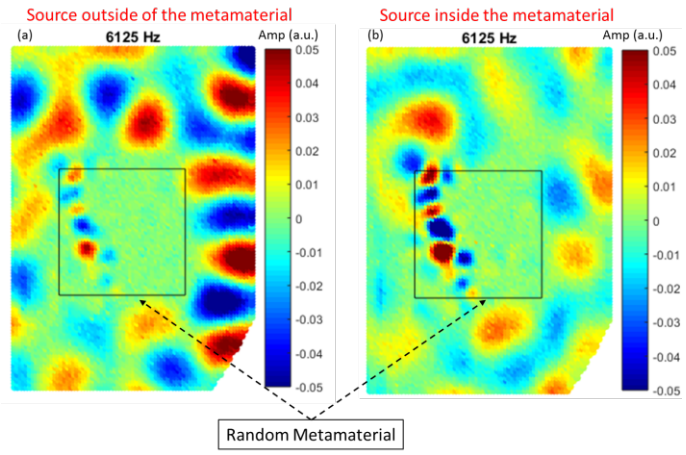

Figure 1.10 – Spatial representation of the Fourier transform (real part) of the wavefield at f = 6125 Hz. The wavefield pattern demonstrates energy leakage at the edge of a stopband at f = 6125 Hz for a source located either outside (a) or inside (b) the metamaterial. Note that the localized mode shape inside the metamaterial (black square) is independent of the source location.

propagation from rod to rod that finally results in a leakage outside the metamaterial region.

A similar effect is shown in Fig. 1.10. The source is either located inside or outside the metamaterial (as in Fig. 1.7), and we choose to display the wavefield at f = 6125 Hz, which corresponds to the start of the stopband (expected at f_0 = 6190 Hz according to the theoretical prediction of Williams et al. [WIL 15]). The wavefield intensity should be very low at this frequency, as attenuation dominates in this frequency band (Fig. 1.4b) and the plate behaves as if it is clamped by the rod anti-resonance (Fig. 1.5e). However, as there is one flexural resonance frequency of the rods nearby (Fig. 1.5b), some of the energy still penetrates into the metamaterial and traverses it from one side to the other. As in Fig. 1.9, the energy flux into the metamaterial appears to be transported from rod to rod through evanescent waves generated at the rod/ plate interface. Note, however, that these trapped waves are not observed around f = 2050 Hz at the start of the first stopband, where there is no flexural resonance frequency.

When the source is located inside the metamaterial, exactly the same field pattern is measured (Fig. 1.10b), which confirms that this localized mode can exist independent of the source excitation. In the past, similar localized modes have been observed

for microwaves scattered by dense and random distributions of local dielectric scatterers [MOR 07, LAU 07]. These results appear to constitute the unambiguous signature of the existence of strongly localized modes in two-dimensional locally resonant metamaterials.

Finally, in Fig. 1.11, we investigate the time-domain effects related to the different quality factors of the flexural and compressional resonances of the rods. As can be seen in Fig. 1.11b (green), compressional resonances have low Q-factors, which mean that they re-inject the energy that they capture on short time scales. Indeed, compressional resonances correspond to a vertical velocity in the rod that couples easily with the vertically polarized A_0 Lamb mode in the plate. On the contrary, flexural resonances show high Q-factors (Fig. 1.11c, green), which means that flexural vibrations are trapped in the rod for longer times before this energy is fully radiated back into the plate. Time-frequency analysis of the signals recorded inside the metamaterial confirms these results. The spectrogram in Fig. 1.11a shows, for example, that at late recording times, there is still higher wavefield intensity around flexural resonances. Moreover, when the dispersion curve is calculated for a finite duration time window in the early part of the recordings, we retrieve the dispersion curve associated with compressional resonances, as described in Fig. 1.4a. However, when the dispersion curve is computed from the same time window shifted to a later reverberation time, the role of the flexural resonances becomes dominant, in agreement with the theoretical predictions from Colquitt et al. [COL 17] for a full-elastic plate-plus-rods system (Fig. 1.5(b, c), blue and red dotted lines).

This frequency-time analysis helps to separate the effects due to compressional resonances from those due to flexural ones. For example, around f = 6125 Hz, the energy leakage inside the metamaterial (Fig. 1.10a) mostly appears after 100 ms of propagation, which represents the time needed to load the high quality factor of the flexural resonance. On the other hand, the monopole created by the source inside the metamaterial at around 6400 Hz (Fig. 1.7b) is instantaneous, and so it should be associated with the low quality factor compressional resonance.

1.5. Conclusion

In this chapter, we have experimentally revisited the multimodal interactions of an aluminum beam 'forest' glued on a thin elastic plate. This multi-resonant medium is a laboratory scale analog of a real forest, which can behave as a seismic metamaterial. For both systems, the resonant cell supports compressional or flexural resonant modes, which interact differently on the wave substrate. Studying the laboratory system gives some clues to the mechanical signature of such a system.

For longitudinal resonances, the driving point impedance of a single rod dictates the homogenized behavior of the aluminum forest. The bandgap and the highly dispersive curve inside the passband are the two main features of this metasurface. Using

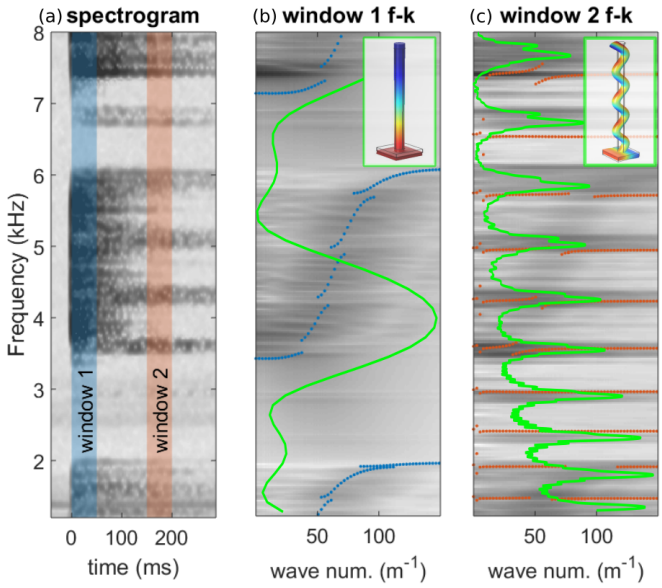

Figure 1.11 – Frequency-time dependence showing the rod resonance contributions to the wavefield. (a) Spectrogram of a signal recorded inside the metamaterial region. (b) Spatial Fourier transform of the wavefield at an early time of propagation (blue colored time window 1 in (a)). The blue dotted line is the predicted dispersion relation for the out-of-plane polarization. (c) Spatial Fourier transform of the wavefield for the late reverberation time (red colored time window 2 in (a)). The red dotted line is the predicted dispersion relation for the in-plane polarization. The associated compressional or flexural motions of the rods are shown in green and are superimposed on the selected time windows, together with relevant examples of modal deformation.

different source locations inside and outside the rod forest helps to quantify these effects. On top of this behavior, the high quality factor flexural resonances add some disturbances, like bandgap leakage with outlandish spatial distribution of the energy.

Finally, the time dependence of the system is studied through short window analysis of the reverberating coda. Directly related to the quality factor of each resonance, we have shown that the hybridization of the flexural waves inside the metamaterial evolve over space and time.

1.6. Bibliography

[ACH 13] ACHAOUI Y., LAUDE V., BENCHABANE S., KHELIF A., "Local resonances in phononic crystals and in random arrangements of pillars on a surface", *Journal of Applied Physics*, vol. 114, num. 10, Page104503, AIP, 2013.

[BRÛ 14] BRÛLÉ S., JAVELAUD E., ENOCH S., GUENNEAU S., "Experiments on seismic metamaterials: molding surface waves", *Physical review letters*, vol. 112, num. 13, Page133901, APS, 2014.

[CHR 12] CHRISTENSEN J., DE ABAJO F. J. G., "Anisotropic metamaterials for full control of acoustic waves", *Physical review letters*, vol. 108, num. 12, Page124301, APS, 2012.

[COL 14] COLOMBI A., ROUX P., RUPIN M., "Sub-wavelength energy trapping of elastic waves in a metamaterial", *The Journal of the Acoustical Society of America*, vol. 136, num. 2, p. EL192–EL198, ASA, 2014.

[COL 16a] COLOMBI A., COLQUITT D., ROUX P., GUENNEAU S., CRASTER R. V., "A seismic metamaterial: The resonant metawedge", *Scientific reports*, vol. 6, Page27717, Nature Publishing Group, 2016.

[COL 16b] COLOMBI A., GUENNEAU S., ROUX P., CRASTER R. V., "Transformation seismology: composite soil lenses for steering surface elastic Rayleigh waves", *Scientific reports*, vol. 6, Page25320, Nature Publishing Group, 2016.

[COL 16c] COLOMBI A., ROUX P., GUENNEAU S., GUEGUEN P., CRASTER R. V., "Forests as a natural seismic metamaterial: Rayleigh wave bandgaps induced by local resonances", *Scientific reports*, vol. 6, Page19238, Nature Publishing Group, 2016.

[COL 17] COLQUITT D., COLOMBI A., CRASTER R., ROUX P., GUENNEAU S., "Seismic metasurfaces: Sub-wavelength resonators and Rayleigh wave interaction", *Journal of the Mechanics and Physics of Solids*, vol. 99, p. 379–393, Elsevier, 2017.

[COW 11] COWAN M. L., PAGE J. H., SHENG P., "Ultrasonic wave transport in a system of disordered resonant scatterers: Propagating resonant modes and hybridization gaps", *Physical Review B*, vol. 84, num. 9, Page094305, APS, 2011.

[DER 01a] DERODE A., TOURIN A., FINK M., "Random multiple scattering of ultrasound. I. Coherent and ballistic waves", *Physical Review E*, vol. 64, num. 3, Page036605, APS, 2001.

[DER 01b] DERODE A., TOURIN A., FINK M., "Random multiple scattering of ultrasound. II. Is time reversal a self-averaging process?", *Physical Review E*, vol. 64, num. 3, Page036606, APS, 2001.

[FAH 04] FAHY F., WALKER J., *Advanced applications in acoustics, noise and vibration*, CRC Press, 2004.

[FAN 06] FANG N., XI D., XU J., AMBATI M., SRITURAVANICH W., SUN C., ZHANG X., "Ultrasonic metamaterials with negative modulus", *Nature materials*, vol. 5, num. 6, Page452, Nature Publishing Group, 2006.

[GUE 07] GUENNEAU S., MOVCHAN A., PÉTURSSON G., RAMAKRISHNA S. A., "Acoustic metamaterials for sound focusing and confinement", *New Journal of physics*, vol. 9, num. 11, Page399, IOP Publishing, 2007.

[LAU 07] LAURENT D., LEGRAND O., SEBBAH P., VANNESTE C., MORTESSAGNE F., "Localized modes in a finite-size open disordered microwave cavity", *Physical review letters*, vol. 99, num. 25, Page253902, APS, 2007.

[LEM 11] LEMOULT F., FINK M., LEROSEY G., "Acoustic resonators for far-field control of sound on a subwavelength scale", *Physical Review Letters*, vol. 107, num. 6, Page064301, APS, 2011.

[LEM 13] LEMOULT F., KAINA N., FINK M., LEROSEY G., "Wave propagation control at the deep subwavelength scale in metamaterials", *Nature Physics*, vol. 9, num. 1, Page 55, Nature Publishing Group, 2013.

[LER 09] LEROY V., STRYBULEVYCH A., SCANLON M., PAGE J., "Transmission of ultrasound through a single layer of bubbles", *The European Physical Journal E*, vol. 29, num. 1, p. 123–130, Springer, 2009.

[LIU 00] LIU Z., ZHANG X., MAO Y., ZHU Y., YANG Z., CHAN C. T., SHENG P., "Locally resonant sonic materials", *science*, vol. 289, num. 5485, p. 1734–1736, American Association for the Advancement of Science, 2000.

[MOR 07] MORTESSAGNE F., LAURENT D., LEGRAND O., SEBBAH P., VANNESTE C., "Direct Observation of Localized Modes in an Open Disordered Microwave Cavity", *Acta Physica Polonica-Series A General Physics*, vol. 112, num. 4, p. 665–672, Warszawa: Panstwowe Wydawnictwo Naukowe, 1970-, 2007.

[PEN 99] PENDRY J. B., HOLDEN A. J., ROBBINS D. J., STEWART W., "Magnetism from conductors and enhanced nonlinear phenomena", *IEEE transactions on microwave theory and techniques*, vol. 47, num. 11, p. 2075–2084, IEEE, 1999.

[PSA 02] PSAROBAS I., MODINOS A., SAINIDOU R., STEFANOU N., "Acoustic properties of colloidal crystals", *Physical Review B*, vol. 65, num. 6, Page064307, APS, 2002.

[ROU] ROUX P., RUPIN M., LEMOULT F., LEROSEY G., COLOMBI A., CRASTER R., GUÉNNEAU S., KUPERMAN W. A., "New Trends Toward Locally-Resonant Metamaterials at the Mesoscopic Scale", World Scientific.

[ROU 18] ROUX P., BINDI D., BOXBERGER T., COLOMBI A., COTTON F., DOUSTE-BACQUE I., GARAMBOIS S., GUEGUEN P., HILLERS G., HOLLIS D. et al., "Toward Seismic Metamaterials: The METAFORET Project", *Seismological Research Letters*, vol. 89, num. 2A, p. 582–593, Seismological Society of America, 2018.

[ROY 00] ROYER D., DIEULESAINT E., "Elastic Waves in Solids I: Free and Guided Propagation, translated by DP Morgan", *Springer-Verlag, New York*, 2000.

[RUP 14] RUPIN M., LEMOULT F., LEROSEY G., ROUX P., "Experimental demonstration of ordered and disordered multiresonant metamaterials for lamb waves", *Physical review letters*, vol. 112, num. 23, Page234301, APS, 2014.

[RUP 15] RUPIN M., ROUX P., LEROSEY G., LEMOULT F., "Symmetry issues in the hybridization of multi-mode waves with resonators: an example with Lamb waves metamaterial", *Scientific reports*, vol. 5, Page13714, Nature Publishing Group, 2015.

[RUP 17] RUPIN M., ROUX P., "A multi-wave elastic metamaterial based on degenerate local resonances", *The Journal of the Acoustical Society of America*, vol. 142, num. 1, p. EL75–EL81, ASA, 2017.

[SMI 00] SMITH D. R., PADILLA W. J., VIER D., NEMAT-NASSER S. C., SCHULTZ S., "Composite medium with simultaneously negative permeability and permittivity", *Physical review letters*, vol. 84, num. 18, Page4184, APS, 2000.

[WIL 15] WILLIAMS E. G., ROUX P., RUPIN M., KUPERMAN W., "Theory of multiresonant metamaterials for A 0 lamb waves", *Physical Review B*, vol. 91, num. 10, Page104307, APS, 2015.